Morpho-topological volume analysis of porous materials for nuclear applications

Romeu Pieritz[a], José Spino[b], Pavel Vladimirov[c], Claudio Ferrero[d]

[a] ARS - Applied Research Solutions, Chirens, France

[b] European Commission, JRC-Institute for Transuranium Elements, Karlsruhe, Germany

[c] Karlsruher Institut für Technologie, Institut für angewandte Materialien, Karlsruhe, Germany

[d] European Synchrotron Radiation Facility (ESRF), Grenoble, France

The filtered medial line operator is a methodological tool for the morphological and topological analysis of reconstructed samples exhibiting either a porosity network or a granular structure such as bead packs. An application example of this methodology is the evaluation of the pore structure and the derived topological parameters of nanocrystalline 4Y-ZrO_2 specimens simulating the high burn-up structure of UO_2 fuel. The data indicate the absence of percolation paths at the experimental resolution, which is a beneficial property in terms of retaining fission gasses during the in-pile operation of the fuel. Furthermore, the analysis revealed a tendency for pore coalescence, which could explain the departure from the ideal behaviour of some physical properties typical of material matrices with a population of merely spherical pores. The same analytical tool is also used to characterise the porosity network created by gas bubbles in neutron irradiated beryllium samples, a material meant to be used for the blanket of the forthcoming generation of Tokamak fusion reactors. In particular, the preliminary results of the quantitative analysis performed on the porosity of the beryllium matrix as well as the initial investigation of its percolation properties are reported.

Keywords: Porous materials; X-ray microtomography; 3D image analysis

1. Introduction

The thermo-mechanical properties of porous media are closely related to the geometrical complexity of the pore network structure. This structure is characterised by geometrical quantities related to the shape of the pores and the surrounding matrix, i.e. the morphology of the investigated samples as well as the physical links between the pores, i.e. the material topology. An analytical method has been continuously developed for more than a decade to enable an efficient description in morphological and topological terms of three-dimensional (3D) micro-structures [1, 2]. A set of geometrical operators was defined in an algorithmic form (discrete geometry) allowing the compaction of the relevant sample information into discrete "skeletons" called medial lines. This approach allows determining a topological distribution function through a network description via sites and bonds as well as shape descriptors to be applied over the generated numerical data. Two examples of use of this analytical framework are reported in the following sections: one is the characterisation of a bulk nanocrystalline material for nuclear reactor applications [3, 4] and the other is the study of the topology of porous networks present in neutron irradiated beryllium in view of important safety aspects related to the construction and operation of the future European Tokamak fusion reactor [5, 6].

2. The analytical framework

2.1. Morphological analysis

The rationale of the computational methodology described in this work was already reported in [7] and references therein. Here we will only summarise the main features of it and add some details which will serve the purpose of better understanding the results shown in Sections 4.1 and 4.2. The morphological analysis of a porous medium aims to evaluate the volume fraction occupied by the solid phase in the whole sample (volume ratio), or equivalently the complementary quantity (void fraction). For this analysis to be carried out, segmented images are hence required. Often it is of paramount importance to detect the spatial arrangement of the

porous phase including possible anisotropies, as well as volume and surface ratios of a two-phase sample. A very fast method with a relatively good control on the errors for measuring volume and surface sizes in the discrete geometry of a 3D computer aided microtomography (CMT) image is counting the individual volume and surface elements [8]. The method is based on the analysis of the voxel neighbourhood, which consists in assigning a label to a voxel at the surface of a given sub-volume by inspecting its 26 surface neighbours, indicating the surface or the volume average as a function of the topology of the surrounding surface elements [9]. The associated surface measure error is thereby estimated to be less than 2 % when calculating distances for relatively large size objects (10 voxel radius or more) [9]. The main phase object radii are found using a 3D discrete distance map [1, 2], representing the maximum spheres inscribed in the non-void volume shapes. The related error can be reduced by a post-processing step to obtain the "real Euclidean radius" (the error being ± 0.5 voxel resolution). This procedure evaluates the real Euclidean distance between each maximum sphere centre, adopting this value as the correct one.

2.2 Percolation Analysis

A percolation path is by definition a channel connecting two opposite "open" surfaces in a solid matrix, and is composed of elements on different size scales able to transport any kind of fluid or gas contributing to determining the micro–macro physical transport/mechanical/electrical properties of a medium. It is characterised by the "percolation threshold" of the void fraction [10–12] which represents the minimum porosity value needed to observe these channels. In other words, the percolation threshold can be defined as the critical fraction of network sites which has to be filled in order to create a continuous path of nearest neighbours from one side to another of a sample of finite size. Determining exact analytical expressions for percolation thresholds remains an open problem, and can be solved only numerically case by case.

At any rate, cracks and local collapses of the solid matrix do not represent percolation elements.

All CMT experiments are intrinsically limited by the spatial resolution, thus the "observed" porosity represents probably only one component (on the micrometric scale) of the total porosity, and hence not the nanometric (or sub-micrometric) porosity. The "effective" percolation path is likely to be composed of the interconnections of objects on different scales. The procedure to identify the percolation clusters candidates is based on the classification of three different types of elements: the "closed" objects, the "open" objects and the "percolation" candidates (which are also "open" objects). It is well known that the percolation analysis results depend critically on the object dimensions and, consequently, on those of a representative region of interest (ROI). In the present study, the ROI is the maximum internal volume enclosed in a regular shape (in this case a rectangular prism) not intersecting the external surfaces of the raw sample. Such a ROI maximises the volume data to analyse and avoids the complexity of the external surfaces of the sample. For the purposes of this investigation one can use the maximum internal rectangular prism because of the stated isotropy of the samples (cf. Section 4).

The closed objects are the elements not touching any of the external surfaces of the explored region of interest (ROI): they are independent pore objects completely enclosed in the bulk matrix. The open objects are objects touching at least one of the external surfaces of the ROI. The percolation candidates are special open elements in contact with two or more external surfaces. The term "candidates" is used here because small artefacts can be located at the surface intersections, and creating false connections, which do not really represent a percolation path. The extremely small volume associated to such objects can however help to identify these cases.

2.3. Topological analysis

The computational procedure used to determine the radii of the individual elements composing a single-phase object, the contact surfaces between these elements and their coordination numbers is implemented via a topological operator called filtered medial line (FML) applied to the entire data

volume and the related graph representation (FML Graph) [2]. The binary data volume is used to generate a discrete distance map, displaying the largest spheres inscribed in the individual objects of the volume.

Primarily integer metrics are employed in imaging techniques, hence several approaches are possible. The most common algorithms make use of truncated metrics (Chamfer metrics) based on a fixed-size mask estimation of the Euclidean metric [13] providing a time-effective calculation of the distance map and graph representations. The discrete distance transform used here is based on the Chamfer distance d_{345} [14]. In order to illustrate the basic principles of the topological operator let us consider the simple example of Fig. 1 where an assembly of 6 spheres is depicted. The first step for the algorithm in order to classify these spheres (main nodes) consists in identifying the connections of the different objects and in building a completely connected skeleton i.e. the medial line (ML), which is obtained by joining the real centres characterised by the Euclidean values of the radii. A segment of the skeleton having a width (diameter) of one voxel is called line or arc. In Fig. 2 the connection nodes on the skeleton of the objects of Fig. 1 are marked in green, whereas the main nodes are in red and the arcs in blue. Part of this technique has been used to determine the distribution of standard Euclidean objects (cubes, spheres, ellipsoids, …) based on the sample topology, and was proven to give an excellent match in terms of the real radii of the reference objects and the final results obtained from the Euclidean evaluation (refinement steps for surface and volume calculations) [15–17]. The automatic identification process of the ML graph would generate a complex, hyper-connected surface, eluding the recognition of simple structures throughout its shape. In order to overcome this limitation, a topological filter is applied, which preserves the initial topological invariant universally known as Euler number or Euler characteristic [13] for every element of the ML network. The resulting variety is the FML, which gives a complete topological description of the set of objects composing a volume. A realistic example of the complexity of a FML model is shown in Fig. 3. Although the graph representation of the FML is only an abstraction, this

procedure was demonstrated to be suitable for the description of 3D images with a large distribution of very fine objects. Figure 3 shows the FML of a real object extracted from a porous network of 24581 individual pores. The porous object referred to in the picture is the one reported in Section 4.1 below.

2.4. The scale problem

The topological analysis (i.e. the FML Graph) of a volume depends to a great extent on the used scale (or voxel resolution) [2]. The analysis of the same object can lead to different results basing on the experimental resolution, as is shown schematically in Fig. 4 (an example for how challenging it might be to represent an object with a poor resolution). In other words, the topological analysis of bulk data is critically dependent on the characteristic length scale of the phase objects, especially when they have the same size as the volume image sampling applied (i.e. the so-called voxel resolution).

The main node representation of an object is also dependent on its own geometry, as presented in Fig. 5. The skeleton of a rectangle (or of a rectangular prism in 3D) coincides almost entirely with the main node element (in red). The circle (or a sphere in 3D) has a complex skeleton but the main node is the centre of the shape (red dot). Generally speaking, the main node is characterised by the "biggest" radius in the skeleton point set. These geometrical relations have an important influence on the overall result [1, 2, 13]. In most of the cases dealing with real complex shapes, the usually large statistics of phase elements tend to smear out special cases with local effects.

3. X-ray measurements: Experimental

The experimental station used to acquire the 3D images presented in Sections 4.1 and 4.2 is the beamline ID19 at the European Synchrotron Radiation Facility (ESRF), Grenoble, France. Details of the experimental rig providing adjustable spatial resolutions which range from 0.2 to

40 μm, depending on the size of the sample, can be found elsewhere [18]. It should be noted that the X-ray energy selected for the sample in Section 4.1 was 34 keV and the detector spatial pixel sampling was 0.28 μm. In order for the sample to be entirely scanned, it had to be vertically translated 3 times, owing to the limited vertical size of the incident beam. As a result the sample was divided vertically in a stack of 4 sub-volumes. Each individual sub-volume was scanned at 1300 angular positions covering a total rotation range of 180 degrees. Dark current measurements and flat field reference images were also taken for electronically denoising and normalising the 2D frames before reconstruction. Differently from the above experiment, the measurements reported in Section 4.2 were performed with various spatial samplings, namely 1.4, 0.3 and 0.2 μm, respectively, using a monochromatic beam of 17.4 keV photon energy. All the other experimental conditions remained however essentially unchanged.

Both experiments produced substantial amounts of data (of the order of one Tb) therefore requiring sophisticated processing, which was performed in the following steps:

- Raw data assembling: normalisation, volume domain decomposition, quality control, data format conversion;
- Tomographic reconstruction, performed using a massively parallelised filtered back-projection algorithm [19].
- Pre-processing of the raw data: grey level correction, object shape correction, morphological and topological filtering, elimination of artefacts (“ring” correction), selection of the region of interest for further processing, etc.;
- Processing: deployment of data for modelling, visualisation, measurement and simulation purposes.

The processed data are in the form of 2D greyscale slices. Using accurately selected threshold values these data were converted into binary images, which are more suitable for the post-processing, as the data are already subdivided into solid and porous phases. The threshold value is chosen based on the frequency (e.g. grey level frequency distribution) preserving the

experimentally observed microporosity. Also, the value is often corrected and adjusted by human inspection to prevent artefacts due to X-ray noise from the experiment and related instrumentation.

Two dimensional data were collected into stacks, thus presenting a 3D distribution of solid material and pores as volume elements (voxels). Neighbouring volume elements containing voids are assumed to belong to one object representing a pore. As mentioned above, volume and surface area of the pores are evaluated as a sum of volumes of all elements belonging to the object and as a sum of the face areas separating void and solid phases, respectively.

4. Applications

4.1. Porous yttria-stabilised zirconia

The release of fission gases (Xe, Kr) into the inner volume of fuel pins in commercial UO_2 light water reactors (LWR) is a key parameter that limits the permanence of the fuel in the reactor. Recent developments at the Institute for Transuranium Elements (ITU), Karlsruhe, have allowed the fabrication of bulk nanocrystalline and porous specimens of yttria-stabilised zirconia $(Y_2O_3)0.04(ZrO_2)0.96$, i.e. 7.3 wt. % of Y_2O_3 in ZrO_2 with a microstructure largely resembling that of the rim material that develops at the periphery of LWR fuel rods at high burn-ups, typically in excess of ~70 GWd/tM [3, 4, 20]. For the fabrication process and the achieved microstructure the reader is referred to Santa Cruz et al. [20]. It should be just reminded that for creating a pore population in the specimens, calibrated PMMA spheres were used as burnable templates. A remarkable feature of this material, very much like the high burn-up structure (HBS), fuel superplasticity and diffusion creep appear to be enhanced due to the presence of nano-sized grains as opposed to the micro-sized grains of the reference unirradiated UO_2 reference material. The equiaxial form of the nano-grains even after large strains and the low stress exponent of the creep rate suggest grain boundary sliding to be the major plastic deformation mechanism. This property is very likely to promote improved

radiation tolerance via enhanced defects recombination and interaction with the grain boundaries. This entails higher burn-ups and, as an immediate consequence, a very beneficial impact on the whole economy of nuclear reactor plants.

The results of the CMT reconstruction and 3D analysis performed on the reconstructed volume of a specimen of Y_2O_3–ZrO_2 and aiming at revealing the underlying pore interconnection paths and pore spacing are reported in the following. In Fig. 6 is depicted the whole irradiated sample (dimensions 197 × 316 × 2900 μm^3) which was cut from a larger chunk of material with tailored pores of nominal radius 1.7–1.8 μm and nominal porosity fraction 0.16. Due to the tensile stress field around the cavities left behind by the burnt-up PMMA spheres, the porous cavities are expected to shrink partially. The boundary surfaces of the sample look somewhat fissured, but the pores are clearly visible. One can also notice the presence of large superficial cracks, some of which can be easily found by visually inspecting the FML graph of Fig. 3. Altogether seven such cracks were detected by the algorithm.

Figure 7 shows the void volume contributions from each individual pore in the solid matrix, as found out by deploying the FML methodology. The diagram includes the porosity which is detected at the sample surface. The sum of all contributions leads to a total volume fraction of 15.63 %, very much in agreement with the nominal value of it. The seven "giant" pores detectable in Fig. 7 are actually the cracks which were found by visual inspection of the reconstructed volume. They constitute 7 % of the totally detected porosity, i.e. 1.05 % of the total sample volume. It should be added that the 140 biggest pores account for 23 % of the total porosity, i.e. 3.45 % of the whole volume.

In Fig. 8, which features the radial size distribution frequency of the pores in the matrix, the cracks and all the other pores attaining the ROI surface are excluded. The remaining pores are thus 20144 and make up 11.63 % of the total volume. It is found that most of the radii are comprised in a region of ± 0.7 μm around an average value of 2.0 μm, which matches up to the nominal pore radius, as scanning electron microscopy (SEM) investigations suggest. The

apparent slight mismatch can be easily explained, inasmuch as SEM is essentially a 2D imaging technique, where spherical objects are transversely cut. Assuming an ideal case of equal spheres of radius R in a volume, the radius distribution of circles obtained by crossing the spheres with an infinitely thin plane is the same for any plane. Taking into account that the geometrical averaging over circles in a plane is equivalent to averaging over plane positions with respect to one sphere, it is straightforward to demonstrate that the resulting cross-section radius has a mean value $R_{CS} = (\pi/4)\ R \approx 0.785\ R$. The non-ideality of the present case seems to suggest the true correction factor for it to be comprised in the interval]0.785, 1[and thereby the good agreement between SEM and tomography assessments to be confirmed.

A shape analysis of the pores was performed and the results are summarised by the sphere shape deviation index histogram, in which the pores are sorted top-down (as in Fig. 7) in the sample volume (Fig. 9). The sphere shape deviation index is the ratio of the pore (i.e. void element) volume to the volume of the maximum sphere inscribed in it. Perfectly spherical void volumes would feature an index equal to unity. A value > 1 implies some elongated shape such as an ellipsoid. Exceedingly large values are indicators of a "crack"-like shape. The distribution presented in Fig. 9 shows a major population of pores with a spherical or almost spherical shape (red line: values around the unity). Some points represent objects with ellipsoidal or more complex shapes (index value > 3). Again, seven objects exhibit a sphere shape deviation index value > 5, i.e. large volumes with comparably small diameters (the aforementioned cracks). The values < 1 pertain to very small objects of a very few voxels, such as for instance small cross-shaped volumes, where the main node sphere can have a larger volume than the computed sum of the voxels belonging to the actual volume. A certain tendency of the pores to exhibit a prolate ellipsoidal form, as a probable result of the conjunction of individual spherical pores, is stated: ~38 % of the cavities have shape indexes larger than 1, clearly indicating coalescence of two or more primary cavities, whereas the percentage of those with shape index larger than 2 does not exceed 9 %.

With regard to the percolation behaviour of the sample under study, it should be remembered that a percolation path is by definition a channel connecting two opposite “open” surfaces in a solid matrix. Owing to the limitation related to the spatial resolution of the tomography experiment at ID19, one cannot hence exclude a priori that the effective percolation paths are composed of links between objects on both the micrometric and the nanometric scales.

Only seven objects were found to be good candidates for representing a local percolation path, but all of them are the above mentioned cracks in the solid matrix. These cracks might have formed during the sample manipulation (cutting) or because of the transport or/and experiment. Bearing this in mind, we can conclude that the observed percolation threshold equals zero. This outcome was confirmed independently by another study using the computational methodology reported in [21]. Further experiments on the nanometric scale are planned and might indeed unveil unexplored percolation paths. Would the present results be confirmed by future analyses, the present HBS dummy material would be assessed to exhibit the capability of retaining the gases in its bulk, as it is demonstrably the case for in-pile HBS fuels with regard to fission gases [20].

For the HBS fuel to be adequately simulated by a model material such as nc-Y_2O_3–ZrO_2, the latter needs to feature a structure of random 'overlapping spherical pores', also known in the literature as 'swiss-cheese' structure. Such a system offers the advantage of remaining gas-tight (i.e. non-percolating) up to void fractions around 0.3. Its physical properties (e.g. hardness, Young’s modulus, compressive strength, thermal and electrical conductivity) deteriorate less markedly with spherical porosity than systems with e.g. ellipsoidal or elongated pores, for which the percolation threshold also drops as the pore geometry departs from the spherical form [3, 4]. The property-vs.-porosity-relations of the HBS dummy material do not match the trends predicted for the HBS-material [20], being closer to the predictions for the large-grain sintered material. The reason for that could be, among other things, due to the formation of local chains of pores (necking) acting on average as elongated cavities, thus weakening the

material matrix. The tomography analysis confirmed that the pore chains occur in this case, as some degree of pore contact and coalescence was stated, with the pore phase behaving rather as a system of slightly elliptical cavities

4.2. Irradiated beryllium

Beryllium is planned to be used in future Tokamak-type fusion reactors as a neutron multiplier to achieve sustainable production of tritium, which will be used as a fuel for the fusion process. As by-products of neutron multiplication, hydrogen and helium isotopes are generated by neutron-induced transmutations in beryllium. Gas atoms trapped in the metal matrix stimulate formation of small bubbles, which grow at high temperatures and form a complicated network of interconnected channels. It was shown by gas thermal desorption experiments [5] that burst releases of tritium and helium occur simultaneously at the same temperature, which might be explained by the formation of channels of pores connecting the bulk grains with the sample surface. This assumption was underpinned by the results of earlier microtomography studies [6] as well as by the reduction of the measured helium content after annealing campaigns above 500 °C and complete release of accumulated helium above 750 °C [22]. The topology of the porosity network is therefore important for the tritium inventory evaluation in irradiated beryllium.

In this work we studied the topology of porosity networks developed in beryllium irradiated at relatively low temperatures (40–50 °C) for a long time and then annealed out-of-pile at a number of temperatures for increasing intervals of time. The aim of this is to get insights into the formation and development of gas driven porosity in irradiated beryllium. The case of low temperature irradiation is very attractive for this purpose as far as no visible bubbles are formed during irradiation. By varying annealing temperature and dwell time, one can follow the development of porosity by making microtomography snapshots at particular stages. As *in-situ* annealing under synchrotron radiation would be rather complicated, we annealed under

vacuum irradiated samples at 850 °C and 1000 °C and dwell times of 0.5, 1, 5 and 10 hours in the Fusion Materials Laboratory (hot cells) at the Karlsruhe Institute of Technology and then scanned these samples at room temperature on ID19 at the ESRF, Grenoble. Besides annealed samples, we used as references one as-irradiated sample and one sample which was neither irradiated nor heated up. One sample was made of industrial grade beryllium similar to that of the irradiated samples. The irradiated samples (S200E Be grade) were irregularly broken fragments of the neutron reflector of the Belgium material testing reactor BR2 with sizes of about 0.5 mm. Approximately 2.2 at. % of helium was accumulated in the samples after 15 years of irradiation.

Unfortunately, after long exposure to synchrotron radiation the inner plexiglass cylinders of the sample holders start to break. As a consequence, not all specimens were measured with all spatial resolutions available (cf. Table 1)

In particular, it was interesting to find under which conditions the interlinked channels developed in the material reaching the outer surface (formation of open porosity). Physically, this is the process triggering a burst gas release from the irradiated samples.

The porosity of the samples was analysed using three classes of pores: closed, open and percolation candidates. The results for all post-processed samples are collected in Table 2.

The preliminary statistical analysis performed for the measurements at 1.4 µm effective pixel size revealed that all samples, except two (p9 - “as irradiated” and p10 - “not annealed”), have isotropic distributions of pores. The samples p9 and p10 show small oscillations in the axial and radial porosity distributions. However, the conclusion about inhomogeneity is certainly affected by the low number of pores found in these samples and, hence, by the larger statistical uncertainty. In fact, the isotropic character of the pore distribution was confirmed for the sample p9 after measurements with 0.3 and 0.2 µm effective pixel size.

We consider first the results measured at 1.4 μm spatial sampling. The vast majority of the pores have sizes comparable with the size of a unitary volume element (voxel). The average cluster size is less than 5 voxels, if the largest percolation clusters are excluded.

It should be noted that percolation clusters are absent only in the case of the "as irradiated" sample (p9) where the total porosity is mainly determined by the "closed" pores. Very low total porosity (0.56 %) was observed in this case. In contrast to that, even at the shortest annealing time and the lowest temperature (0.5 h @ 850 °C) percolation pores are well developed and constitute ~96 % of the total porosity. Under these conditions the percolation cluster contains about 4 million voxels. Its main diameter, determined by the inscription of the maximum sphere, was found to be 2.8 μm. Some pores are exceptionally large and of a shape which is far away from the typical quasi-spherical or lenticular image one is used to seeing when analysing "swiss-cheese" or akin structures. An example of what is meant here is Fig 10, which shows the largest close pore in p9 (the "holes" which can be seen in it are indeed portions of the solid phase) the size of which is 3.5 ‰ of the total ROI volume, which in turn amounts to 0.406 mm^3.

At an annealing temperature of 850 °C the total porosity slightly decreases with increasing annealing time. This behaviour is unexpected, but taking into account the small value of the porosity decrease (2.5 %) we suppose that this might be related to the sample-to-sample statistical variations. This suggestion is also supported by the fact that the total porosity of the same sample can vary within 2.4 % when calculated from data measured with different spatial resolutions. After 1000 °C annealing, porosity is well developed already after 0.5 h and does not change significantly after 1 h of annealing. After 5 hours of annealing, however, the swelling shows an abrupt increase and reaches about 35 %.

In the investigated material the percolation clusters look more like random agglomerations of pores (see one example in Fig. 11) rather than the open channels found in [6] (cf. Fig. 2

therein). Part of the micro-crack going through the whole ROI can be seen on the right hand side of the figure.

5. Conclusions

The analytical framework reported above appears to be a versatile tool for analysing the morphology and the topology of porous biphasic materials. Irrespective of the density, shape and porosity network complexity of the investigated samples the proposed medial line skeleton algorithm, coupled with the relevant volumetric information extracted through a volume-surface integration method basing on the analysis of voxel neighbourhoods appears to provide a useful computational tool to examine sub-micrometric details of matter with satisfactory precision. It helps in unveiling details which contribute to the understanding of the physical behaviour of porous substances such as the HBS dummy material and characterises statistically their percolation behaviour. The satisfactory comparison with the experimental results from other techniques (cf. SEM) corroborates the reliability of the chosen computational approach and encourages its deployment in safety related matters, as is the case for nuclear fuels and neutron irradiated beryllium in fusion reactors.

The authors are deeply thankful to SCK-CEN colleagues for providing the irradiated beryllium material for this study. They are also greatly indebted to Elodie Boller (ESRF Grenoble) and Timm Weitkamp (SOLEIL Paris) for their help in setting up the experiments described in the text.

References:

[1] R.A. Pieritz, Development of the Medial Line Graphics and the Connected Region Threshold Techniques Applied to the Geometrical Porous Media Characterization, Master in Sciences and Engineering Thesis, Federal University of Santa Catarina, Brazil (1994).

[2] R.A. Pieritz, Modélisation et Simulation de Milieux Poreux par Réseaux Topologiques, PhD Thesis, Université Joseph Fourier, Grenoble (1998).

[3] J. Spino, J. Rest, W. Goll, C. T. Walker: J. Nucl. Mater. 346 (2005) 131.

[4] J. Spino, A. D. Stalios, H. Santa Cruz, D. Baron: J. Nucl. Mater. 354 (2006) 66.

[5] E. Rabaglino, C. Ronchi, A. Cardella: Fusion Eng. Des., 69 (2003) 455.

[6] E. Rabaglino, J. Baruchel, E. Boller, A. Elmoutaouakkil, C. Ferrero, C. Ronchi, T. Wiss: Nucl. Instrum. Meth. B 200 (2003) 352.

[7] R. A. Pieritz, J. Reimann, C. Ferrero: Adv. Eng. Mater. 13 (2011) 145.

[8] F. Flin, R.A. Pieritz, J.B. Brzoska, D. Coeurjolly, B. Lesaffre, C. Coléou, P. Lamboley, O. Teytaud, G. Vignoles, J.F. Delesse: IEEE Trans. on Image Processing 14 (2005) 585.

[9] J.M. Barnola, R.A. Pieritz, C. Goujon, P. Duval, E. Boller: Proc. XIII Glaciological Symposium, St. Petersburg, Russia (2004) 80.

[10] J. W. Essam: Rep. Prog. Phys. 43 (1980) 833.

[11] D.Stauffer, A.Aharony: Introduction to Percolation Theory, Taylor & Francis, London (1994).

[12] A. Kantzas, I. Chatzis, Chem. Eng. Comm., 69 (1988) 191.

[13] J.M. Chassery, A. Montanvert: Géométrie discrète en analyse d'images, Hermes, Paris (1991).

[14] J.B. Brzoska, B. Lesaffre, C. Coléou, K. Xu, R.A. Pieritz, Eur. Phys. J. AP 7 (1999) 45

[15] J. Reimann, R.A. Pieritz, M. Di Michiel, C. Ferrero: Fus. Eng. and Design 75-79 (2005) 1049.

[16] J. Reimann, R.A. Pieritz, M. Di Michiel, C. Ferrero, R. Rolli: Fus. Eng. and Design 83 (2008) 1326.

[17] A. Möslang, R.A. Pieritz, E. Boller, C. Ferrero: J. Nucl. Mat. 386–388 (2009) 1052.

[18] T. Weitkamp, P. Tafforeau, E. Boller, P. Cloetens, J.-P. Valade, P. Bernard, F. Peyrin, W. Ludwig, L. Helfen, J. Baruchel: AIP Conf. Proc. (ICXOM20) 1221 (2010) 33.

[19] S. Chilingaryan, A. Mirone, A. Hammersley, C. Ferrero, L. Helfen, A. Kopmann, T. dos Santos Rolo, P. Vagovic: IEEE Trans. Nucl. Science 58 (2011) 1447.

[20] H. Santa Cruz, J. Spino, G. Grathwohl: J. Eur. Cer. Soc. 28 (2008) 1783.

[21] J. Ohser, C. Ferrero, A. Rack, O. Wirjadi, A. Kuznetsova, J. Düll: Int. J. Mat. Res., this issue.

[22] A. Leenaers, G. Verpoucke, A. Pellettieri, L. Sannen, S. Van den Berghe: J. Nucl. Mater., 372 (2008) 256.

Correspondence address:

Dr. Claudio Ferrero

ESRF, BP 220 – F-38043 Grenoble cedex, France

Tel.: 0033476882370

Fax: 0033476882542

e-mail: ferrero@esrf.eu

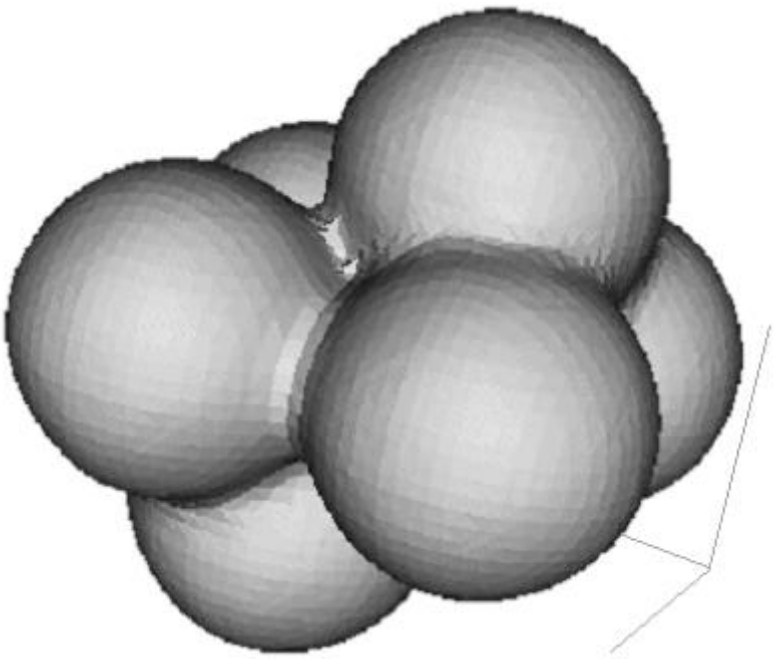

Fig. 1. 3D rendition of an arrangement of six spheres assembled in a cluster .

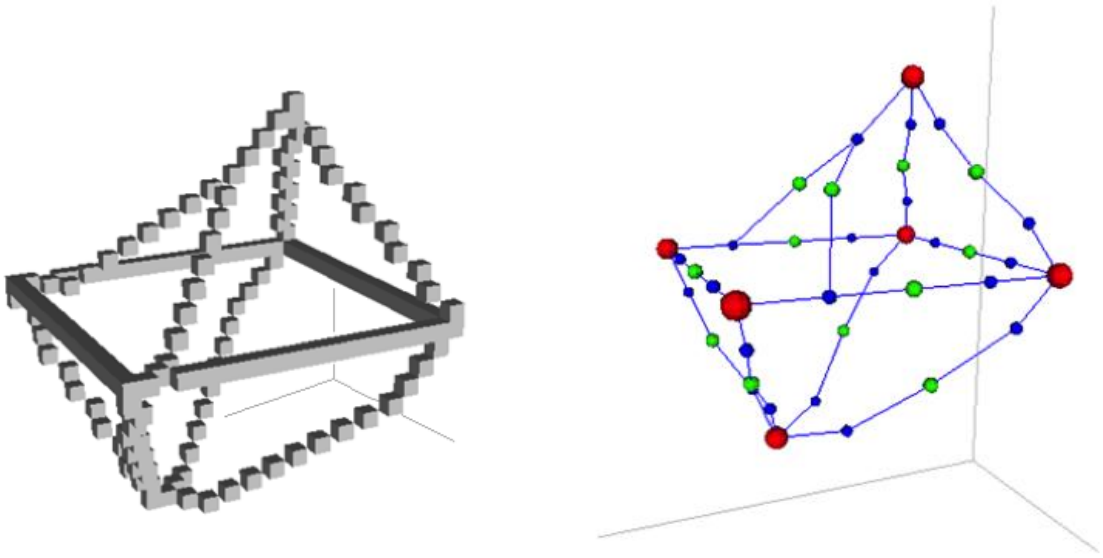

Fig. 2. The connected medial line skeleton of the six spheres of Fig. 1 (left) where the voxels are represented by the cubes in grey. The medial line graph is presented on the right, where the main nodes are in red and the connection nodes in green.

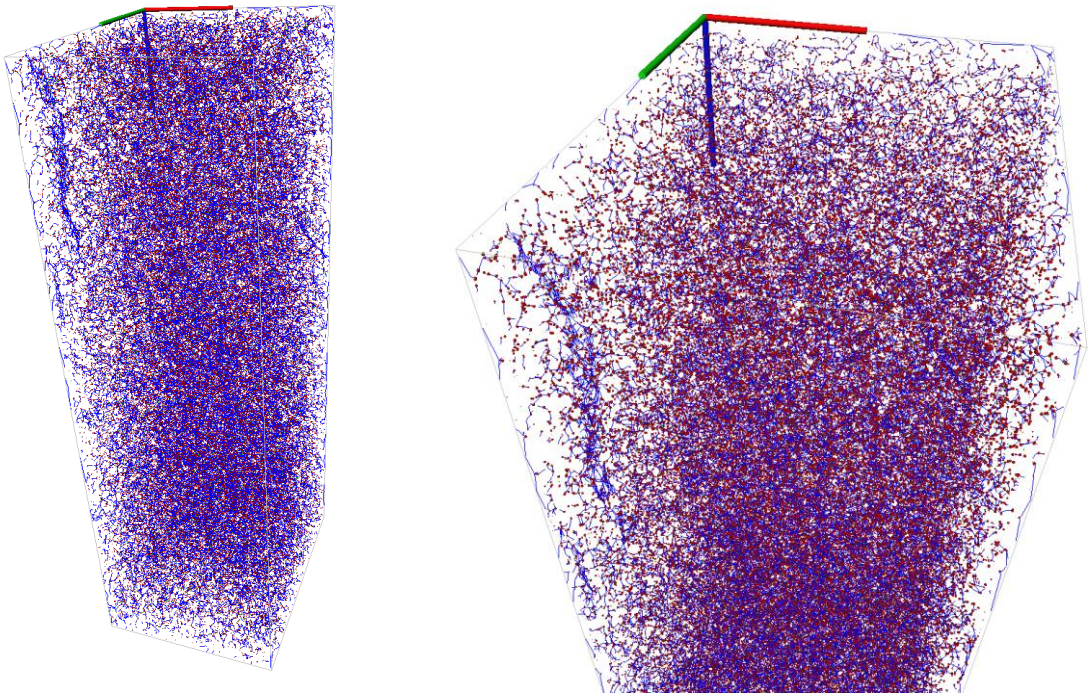

Fig. 3. 3D rendition of the FML graph of a porosity network of 24 581 individual pores (main nodes in red and connection nodes in blue (left) and detailed view (right). The connection nodes are 197 633. The depicted ROI refers to the sample described in section 4.1 (s. also Fig. 6). The ROI sizes are $1.5 \cdot 10^{-4} \times 2.03 \cdot 10^{-4} \times 5.1 \cdot 10^{-4}$ m^3 (i.e. a volume of $1.64 \cdot 10^{-11}$ m^3).

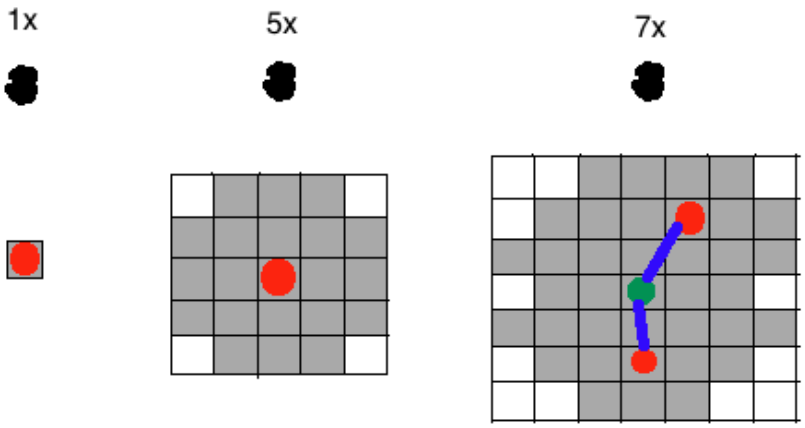

Fig. 4. The same object represented by different skeletons on different scales (voxel resolution), voxel resolution from 1× to 7×. The main nodes are in red, connection nodes in green and connection lines in blue.

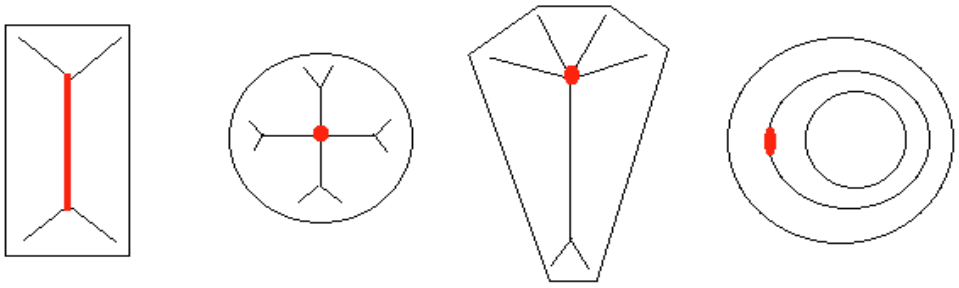

Fig. 5. The different main node 2D shapes (in red) as a function of the geometry of the object and the skeleton (black lines): a point for a circle and a "donut" (i.e. ring) and a line for a square or rectangle. The fourth drawing represents a shape with variable main diameter and the main node (red point) is located where the diameter is at a maximum.

Fig. 6. 3D rendering view of the entire Y_2O_3-ZrO_2 sample after pre-processing (reconstructing and assembling) – voxel resolution: 0.28 μm, total volume: $8.44 \cdot 10^{-11}$ m^3.

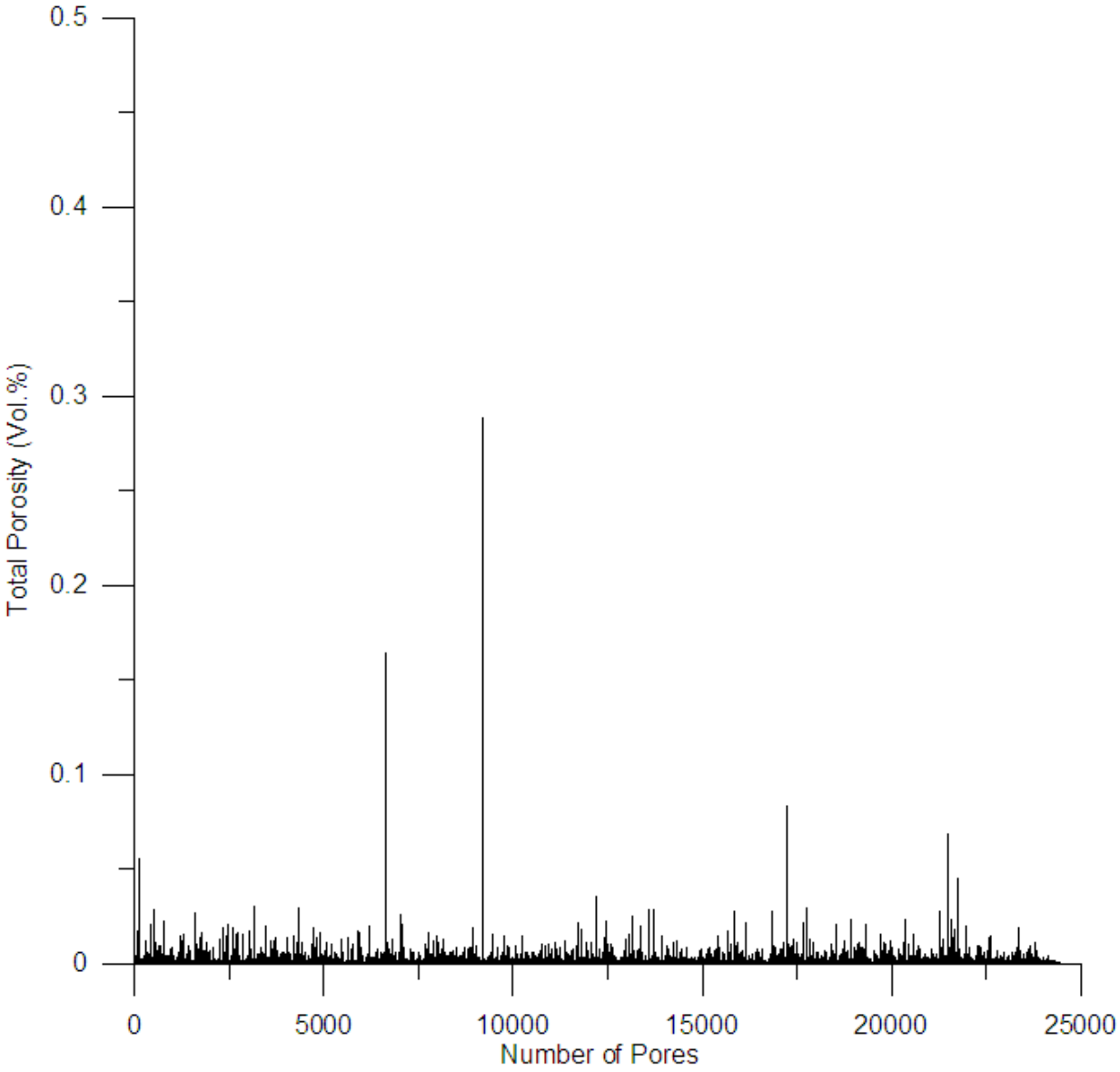

Fig. 7. Volume % of the total porosity for each individual pore in the ROI of Fig. 3. The pores are sorted along the vertical axis of the sample, from the top to the bottom of it.

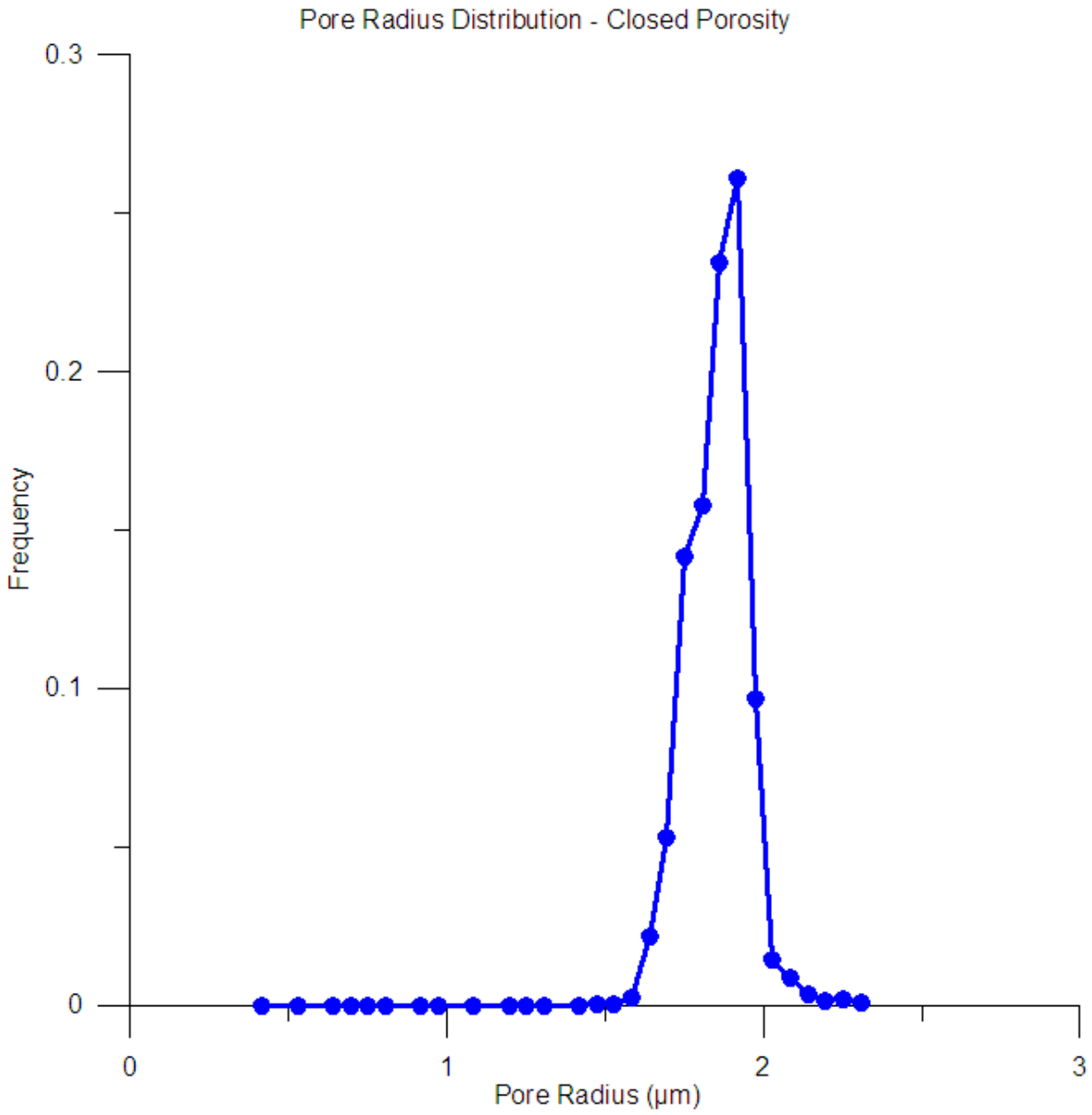

Fig. 8. The closed porosity radius distribution in the ROI of Fig. 3 – 20 144 independent pores (not in contact with the sample external surface – 11.63 % of the ROI volume).

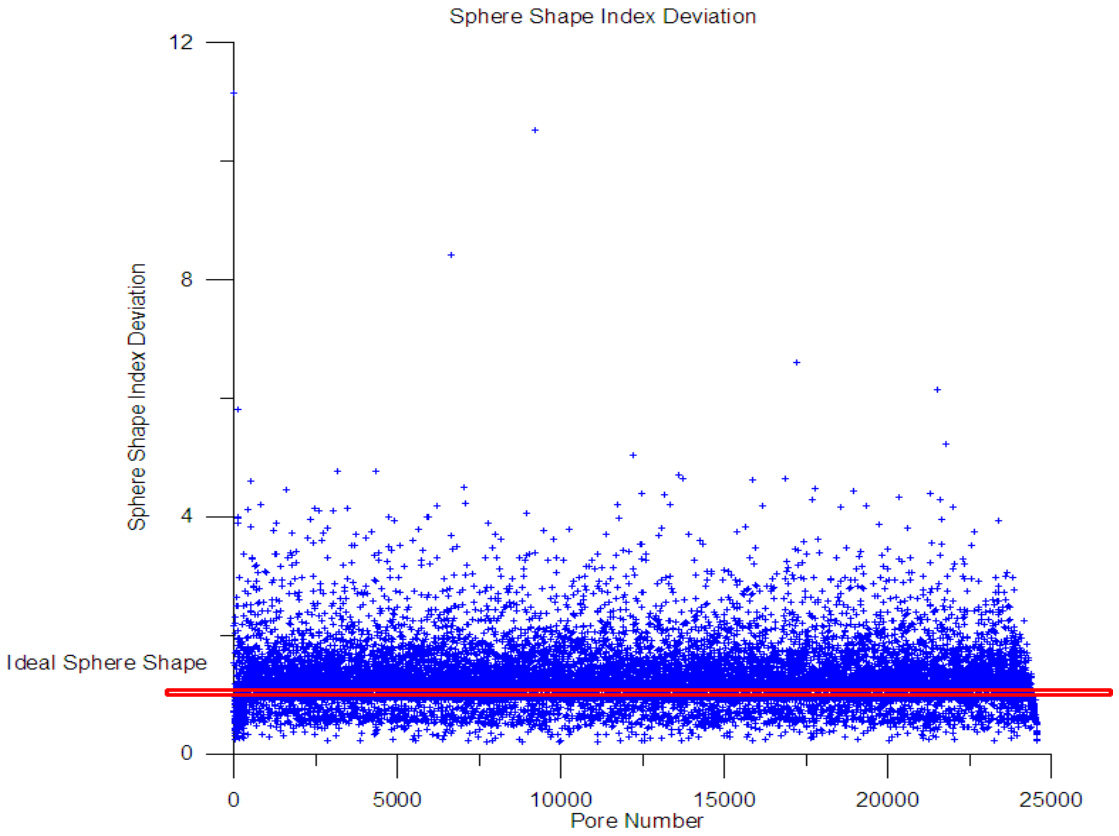

Fig. 9. The sphere shape deviation index computed for all porosity objects in the ROI of Fig. 3 – the red line represents the ideal sphere case.

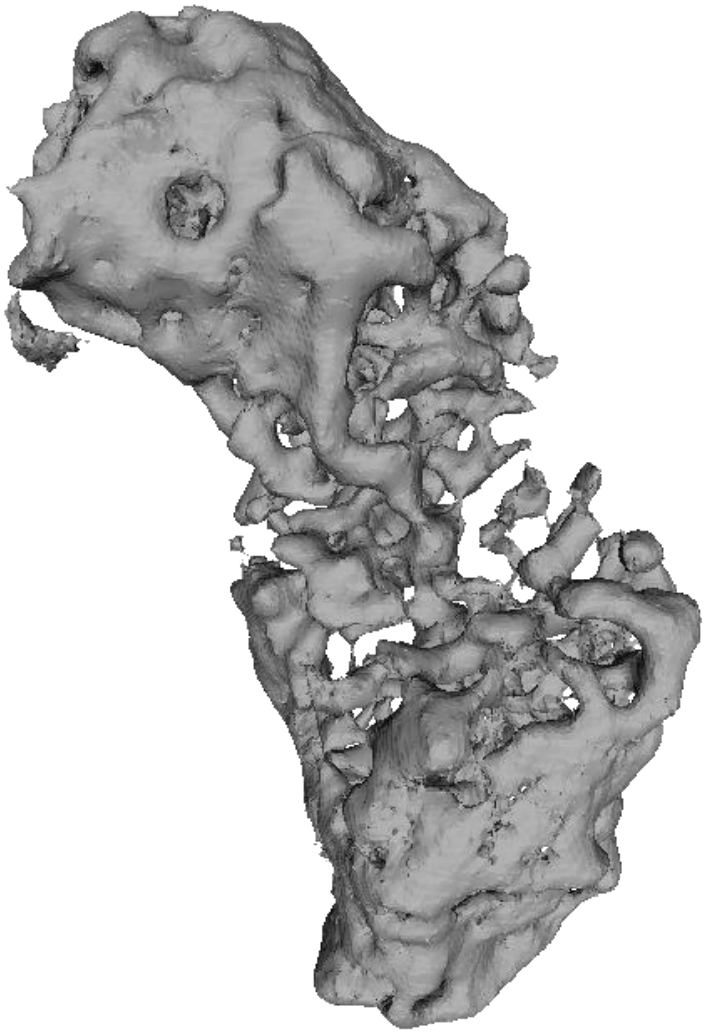

Fig. 10. 3D view of the surface of the biggest pore inside the porosity network of sample p9 (total number of 181 351 pores), The displayed pore contains 193 508 voxels, inside a ROI of 104 × 171 × 152 voxel. The pixel (or voxel) resolution is 0.2 μm

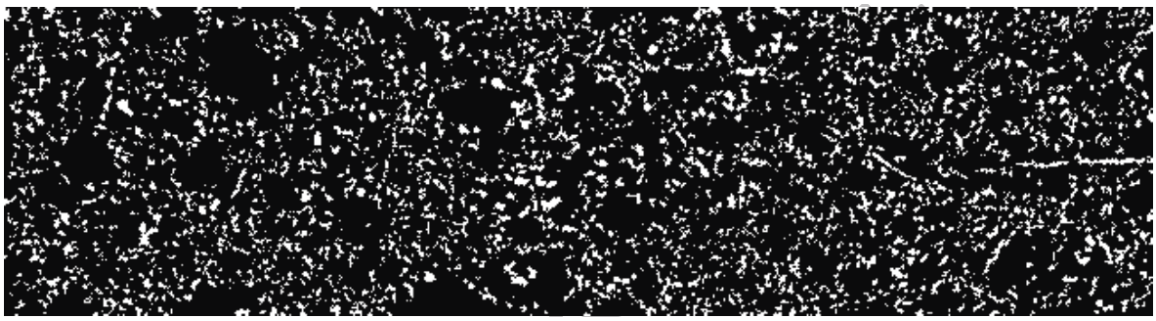

Figure 11. Example of a horizontal section of the largest percolation (in 3D) object (white-pore, black-solid) in the sample p1 measured with pixel resolution 1.4 μm. The section dimensions are $9.07 \cdot 10^{-4} \times 2.44 \cdot 10^{-4}$ m^2

Sample	Conditions	Voxel size (µm)		
		1.4	0.3	0.2
p1	0.5 h @ 850 °C	✓		
p2	1 h @ 850 °C	✓	✓	✓
p3	5 h @ 850 °C	✓	✓	✓
p4	10 h @ 850 °C	✓		
p5	0.5 h @ 1000 °C	✓		
p6	1 h @ 850 °C	✓		
p7	5 h @ 850 °C	✓	✓	
p8	10 h @ 850 °C	✓	✓	✓
p9	as irradiated	✓	✓	✓
p10	unirradiated	✓	✓	✓

Table 1: The investigated beryllium samples with their parameters

Sample	Porosity (vol.%)				Specific Surface (μm^{-1})
	Total	Closed	Open	Percolation	
p1 - 1.4 µm	18.09	0.56	0.17	17.36	0.127
p2 - 0.2 µm	17.83	3.19	0.77	13.86	0.376
p2 - 0.3 µm	19.42	3.47	0.71	15.24	0.351
p2 - 1.4 µm	17.20	0.85	0.14	16.21	0.121
p3 - 1.4 µm	15.71	2.65	0.38	12.69	0.106
p5 - 1.4 µm	18.83	1.05	0.15	17.62	0.124
p6 - 1.4 µm	18.88	1.15	0.26	17.47	0.121
p7 - 1.4 µm	34.97	0.15	0.01	34.81	0.190
p9 - 0.2 µm	0.24	0.22	0.01	0.001	0.006
p9 - 0.3 µm	0.23	0.22	0.02	0.001	0.005
p9 - 1.4 µm	0.56	0.53	0.03	0.001	0.003
p10-1.4 µm	1.42	1.26	0.15	0.003	0.010

Table 2: Porosity and specific surface of the investigated beryllium samples.